PCCP

PAPER

Cite this: Phys. Chem. Chem. Phys., 2017, **19**, 25970

Mechanism of ultrafast non-reactive deactivation of the retinal chromophore in non-polar solvents†

M. Mališ,‡[ab] J. Novak,‡[a] G. Zgrablić,*[cd] F. Parmigiani[cef] and N. Došlić *[a]

Received 17th May 2017,
Accepted 14th September 2017

DOI: 10.1039/c7cp03293e

rsc.li/pccp

The photoisomerization of the all-*trans* protonated Schiff base of retinal (SBR$^+$) in solution is highly inefficient. The present theoretical and experimental investigation aims at disclosing the mechanisms of ultrafast, non-reactive relaxation of SBR$^+$ that lead to the drastic decrease in the isomerization yield in non-polar solvents. Our pump–probe measurements demonstrate the sensitivity of the all-*trans* SBR$^+$ excited-state dynamics on the electrostatic interaction with the surrounding counterions and the crucial importance of the chromophore microenvironment. Our computational study focuses for the first time on the retinal chromophore–counterion pairs that are formed in non-polar solvents. By employing TDDFT-based nonadiabatic dynamics simulations and ADC(2) reaction paths calculations we found that internal conversion from the initially excited state to an inter-molecular charge transfer state with excitation localized on the counterion, leads to dissociation of the chromophore–counterion pair and to the abortion of isomerization. Barriers to conical intersection with the inter-molecular charge transfer state were found in the range 0.42–0.67 eV at the ADC(2) level. The existence of a barrier along the non-reactive relaxation pathways explains the observation that in solution the excitation on the blue edge of the SBR$^+$ absorption leads to decrease in the isomerization yield with respect to the excitation at the red edge.

1 Introduction

The photocycle of microbial rhodopsins begins with the ultrafast all-*trans* to 13-*cis* isomerization of the protonated Schiff base of retinal (SBR$^+$).[1,2] The photoisomerization of all-*trans* SBR$^+$ occurs regiospecifically around the $C_{13}{=}C_{14}$ double bond. In the archetypical bacteriorhodopsin (bR) the reaction takes place on a sub-picosecond timescale[3–5] with an efficiency approaching 65%.[6] In solution, the performance of the reaction is drastically reduced.[7–9] In contrast to the protein environment, the decay of the first excited electronic state (S_1) of all-*trans* SBR$^+$ in solution is multiexponential.[10–12] This originates from a fast non-reactive channel operating on the femtosecond-to-picosecond time scale and from another, slower, non-reactive, channel ($\tau > 5.0$ ps) both competing with the reactive (photoisomerization) channel ($2.8 < \tau < 3.9$ ps) and leading to an efficiency bottleneck. In particular, the fast non-reactive relaxation is the dominant mechanism of deactivation of all-*trans* SBR$^+$ in non-polar solvents, accounting for almost 60% of deactivation events in cyclohexane and 21% in dichloromethane (DCM).[12] Recently a new insight into the photoisomerization dynamics in solution was obtained from a systematic study of the natural and synthetically modified all-*trans* retinal chromophores.[13–15] This includes the striking observation that structural changes that decrease the excited state lifetime lead also to decrease of the quantum yield. The finding of Bassolino *et al.*[14] contrasts previous assumptions that a fast excited state decay implies a barrierless photoisomerization coordinate, but agrees with our previous measurements indicating that the fastest relaxation mechanism is actually non-reactive.[12] In a very recent work, experiments were performed on a modified 11-*cis* chromophore in MeOH.[15] A reduction in excited state lifetime was observed, but not a decrease in the isomerization yield. This indicates that the long-lived excited state population does not undergo isomerization (slow non-reactive channel) and that isomerization may be an intrinsic property of the chromophore only enhanced by the protein environment.[15] The fast non-reactive relaxation channel was not observed in this system.

Altogether, even though a great effort has been directed to understanding the photodynamics of SBR$^+$ in solution, the

---

[a] Department of Physical Chemistry, Ruđer Bošković Institute, Bijenička cesta 54, 10000 Zagreb, Croatia. E-mail: nadja.doslic@irb.hr
[b] Centre Européen de Calcul Atomique et Moléculaire, École Polytechnique Fédérale de Lausanne, Avenue Forel 2, 1015 Lausanne, Switzerland
[c] Elettra-Sincrotrone Treste, T-ReX Laboratory, Strada Statale 14-km 163.5 in AREA Science Park 34149 Basovizza, Trieste, Italy. E-mail: goran.zgrablic@elettra.trieste.it
[d] Politehnika Pula, Riva 6, 52000 Pula, Croatia
[e] Department of Physics, Università degli Studi di Trieste, I-34127 Trieste, Italy
[f] International Faculty, University of Cologne, Albertus-Magnus-Platz, 50923 Cologne, Germany

† Electronic supplementary information (ESI) available. See DOI: 10.1039/c7cp03293e

‡ Equally contributing authors.

mechanisms that interdict the reaction and their dependence on the solvent properties are largely unknown.[11–18] The aim of this work is to disclose these mechanisms.

From gas-phase studies it is known that the photoisomerization dynamics of SBR^+ takes place on the S_1 state and is mediated by an extended seam of conical intersections (CI) between S_1 and the electronic ground state (S_0).[19–23] In solution, the protonation of the Schiff base is ensured by a 3–5 fold excess of strong acid. In such conditions the electrostatic interaction of SBR^+ with the counterions (for example, acetate) and the solvent is expected to affect the photoisomerization dynamics.[24–29] The strong electrostatic effect stems from the redistribution of charge in the S_1 state in which positive charge migrates toward the β-ionone ring. Thus, the position of the negatively charged counterions along the SBR^+ backbone regulates the amount of destabilization of the S_1 state.[18,24,25]

In this work we focus on the counterion effect and report on all-*trans* *n*-butylamine SBR^+ ($n SBR^+$) excited state lifetime measurements in DCM as function of trifluoroacetic acid (TFA) concentration. The experimental data are then compared with surface hopping quantum/classical mechanics nonadiabatic dynamics simulations and *ab initio* reaction path calculations of the complex chromophore–counterion pairs in solution. This joint investigation discloses a counterion sensitive mechanism that might be responsible for the fast non-reactive deactivation of all-*trans* $n SBR^+$ in non-polar solvents.

2 Methods

2.1 Experimental

Transient absorption spectra were collected in the standard pump–probe (PP) configuration whose time resolution was ~85 fs across the full spectral range while shot-to-shot detection ensured very low noise $<3 \times 10^{-4}$ OD. The output of 1 kHz regenerative amplifier was doubled to obtain pump pulses (400 nm, ~60 fs). Part was used for generation of the supercontinuum white light probe in 2 mm thick CaF_2 crystal. The transmitted probe and reference beams were detected in the shot-to-shot scheme by using two Si diode array spectrographs covering the range from 350 to 950 nm.

The spectra were collected at first for the chromophore to TFA molar ratio (C/A ratio, *i.e.* chromophore-to-acid ratio) of 1 : 1 delivering $[n SBR^+ TFA^-]$. The five consecutive scans lasted in total less than 15 minutes to assure that concentration of the all-*trans* isomer decreases less than 1%. Immediately after the first group of scans the solution was titrated in order to obtain a chromophore/acid (C/A) ratio of 1 : 2 yielding $[n SBR^+ TFA^-]TFA$ and the spectra were again collected. Finally, before the third group of scans the solution was again titrated to obtain the C/A ratio of 1 : 4 yielding again $[n SBR^+ TFA^-]TFA$. The same experimental protocol was followed both for DCM and dimethyl sulfoxide (DMSO), solvents in which $n SBR^+$ was dissolved.

2.2 Computational

Optimized structures of $[n SBR^+ TFA^-]$ and $[n SBR^+ TFA^-]TFA$ in DCM and the relevant molecular orbitals are given in the ESI.† Electronic structure calculations were performed with the quantum chemistry packages Turbomole 6.4.[30]

2.2.1 Ground state. We used two computational approaches to describe the structure and dynamics of $[n SBR^+ TFA^-]$ and $[n SBR^+ TFA^-]TFA$ in the electronic ground state. On the one hand we used the conductor like screening model, COSMO,[31] to optimize the ion pairs geometries, and on the other hand the two-layer ONIOM (QM:MM) scheme was employed.[32–35] In the former geometry optimizations with default parameters for DCM, ACN and DMSO were performed using density functional theory (DFT). The PBE0 functional[36,37] and TZVP[38] and cc-pVDZ[39] basis sets were used.

In the ONIOM extrapolation scheme the ground state energy is defined as

$$E^{\mathrm{ONIOM}} = E^{\mathrm{high}}_{\mathrm{model}} + E^{\mathrm{low}}_{\mathrm{real}} - E^{\mathrm{low}}_{\mathrm{model}}$$

where $E^{\mathrm{high}}_{\mathrm{model}}$ is the energy of the model system, a subsystem of the real (entire) system, computed at a high (QM) level of theory. In our case the chromophore–counterion pairs $[n SBR^+ TFA^-]$ and $[n SBR^+ TFA^-]TFA$ constituted the model system. The solvent molecules (real–model system) were described using a low level (MM) method. The extrapolation scheme is also used to compute the ONIOM gradients. The QM part was computed at the DFT level with PBE/TZVP,[40,41] whereas the general Amber force field (GAFF)[42] was used to describe the MM part.[43] Ground state force field parameters for $n SBR^+$, DCM, TFA and TFA^- were estimated using the antechamber module of the Amber suite.[44] The electrostatic embedding scheme was employed to describe the polarization of the model system by the solvent.[34] In all simulations periodic boundary conditions were applied.

To investigate how the polarity of the solvent influences the stability of chromophore–counterion pairs, dynamics simulations were performed in both, polar (DMSO, ACN) and non-polar (DCM) solvents. The two model systems, $[n SBR^+ TFA^-]$ and $[n SBR^+ TFA^-]TFA$, were pre-optimized and embedded in $54 \times 54 \times 54$ Å^3 cubic boxes of DCM (DMSO, ACN). After the initial classical constrained minimization to avoid unnatural close contacts between solute and solvents, 20 ps long *NVT* and 100 ps *NPT* QM/MM equilibrations were performed, followed by the 10 ps production run on the RI-PBE/TZVP//GAFF level of theory. From these 10 ps long trajectories, coordinates and velocities were extracted randomly in windows of 100 fs starting after 2 ps and used as initial conditions for the excited state nonadiabatic dynamics simulations (*vide infra*). Structures were used to compute the excitation spectra.

Two methods were employed to study the mechanisms of excited state deactivation of $[n SBR^+ TFA^-]TFA$ and $[n SBR^+ TFA^-]$ in solution. First, we employed ONIOM-based surface-hopping nonadiabatic (NA) dynamics simulations at the TDDFT level. The aim of these calculations was to explore the range of possible deactivation mechanism active in solution. Subsequently, the feasibility of these mechanisms was investigated using reaction path calculations with the more accurate algebraic diagrammatic construction of second order method (ADC(2)).[45–48] In the last couple of years, the ADC(2) method, which is a correlated single reference method, has been extensively used for studding excited states structure and dynamics of complex molecular systems[49–52] including the reaction pathways of a retinal chromophore model.[53] In terms of accuracy, ADC(2) is comparable to the coupled cluster singles and doubles (CC2) method.

2.2.2 Nonadiabatic dynamics. In recent years different QM/MM variants of NA dynamics, including ONIOM (QM:MM), have been successfully applied to complex photoexcited systems.[54–62] Briefly, in surface-hopping NA dynamics the nuclei obey classical equations of motion

$$\boldsymbol{m}\frac{\mathrm{d}^2\boldsymbol{R}(t)}{\mathrm{d}t^2} = -\nabla V_{\mathrm{el}}^{i}(\boldsymbol{R}(t))$$

where $\nabla V_{\mathrm{el}}^{i}(\boldsymbol{R}(t))$ is the gradient of the currently populated electronic state *i*. The electrons are described quantum mechanically. The electronic wave function, $|\Psi(\boldsymbol{r};\boldsymbol{R}(t))\rangle$, which depends on the electronic coordinates $\boldsymbol{r}$ and parametrically on the nuclear coordinates $\boldsymbol{R}(t)$, is expanded in a set of *N* adiabatic electronic states $|\psi_i(\boldsymbol{r};\boldsymbol{R}(t))\rangle$, $i = 1,\ldots, N$ with time-varying coefficients $C_i(t)$

$$|\Psi(\boldsymbol{r};\boldsymbol{R}(t))\rangle = \sum_{i=1}^{N} C_i(t)|\psi_i(\boldsymbol{r};\boldsymbol{R}(t))\rangle.$$

The time evolution of the coefficient is given by

$$i\hbar\frac{\mathrm{d}C_i(t)}{\mathrm{d}t} = C_i(t)V_{\mathrm{el}}^{\mathrm{i}} - i\hbar\sum_{j} C_j(t)D_{ij}$$

where V_{el}^{i} is the adiabatic energy of the *i* electronic state, and

$$D_{ij} = \int \psi_i(\boldsymbol{r};\boldsymbol{R}(t))\frac{\partial}{\partial t}\psi_j(\boldsymbol{r};\boldsymbol{R}(t))\mathrm{d}r$$

is the element of the nonadiabatic coupling matrix. In Tully's surface hopping[63] the probability of change from the currently occupied state *i* to the state *j* depends on the expansion coefficients and the NA coupling D_{ij} between the states. Thus, three quantities are needed in dynamics simulations: the excitation energies, gradients and the nonadiabatic coupling matrix. In the ONIOM approach, excitation energies, *i.e.*, energy differences between two potential energy surfaces at a particular molecular geometry, are computed as[62,64,65]

$$\Delta E^{\mathrm{ONIOM}} = E^{\mathrm{S}_n,\mathrm{ONIOM}} - E^{\mathrm{S}_0,\mathrm{ONIOM}} = \Delta E^{\mathrm{high}}_{\mathrm{model}} + \Delta E^{\mathrm{low}}_{\mathrm{real}} - \Delta E^{\mathrm{low}}_{\mathrm{model}}$$

where S_0 and S_n refer to the electronic ground and *n*th excited state, respectively. If the excitation is localized on the model system then the ONIOM excitation energy can be simplified as

$$\Delta E^{\mathrm{ONIOM}} = \Delta E^{\mathrm{high}}_{\mathrm{model}}.$$

Within this constrained low-level state (CLS) approximation excited state calculation need to be performed only for the model system.[65] The same approximation is used for the computation excited state gradients and the nonadiabatic couplings.

Owing to the size of our model systems, NA dynamics simulations were performed in the framework of TDDFT. This means that the computation of the nonadiabatic couplings requires first the construction of an 'auxiliary' wave function, which is actually an expansion in spin-adapted single-excitation configurations (CIS) built from Kohn–Sham (KS) spin orbitals[66–68] and then the evaluation of overlaps of these CIS wave functions at two steps in the dynamics. The required molecular orbital and CIS coefficients were obtained from Turbomole, while an in-house software was used to compute the NA couplings.[69–72]

Initial conditions for NA dynamics comprise coordinates and velocities extracted from the 10 ps production phase ground state QM/MM trajectory. TDDFT calculations were performed using PBE0 functional[37,40,41] and the relatively modest SVP basis set. The method was selected after comparing vertical excitation energies and the physical character of low-lying excited states for a number of structures obtained from ground state RI-PBE/TZVP//GAFF trajectories. Classical equations of motion were integrated in steps of 0.5 fs using the velocity Verlet algorithm. The Runge–Kutta method was used to integrate the time-dependent Schrödinger equation in time steps of 5×10^{-5} fs. The PBE0/SVP//GAFF NA trajectories were propagated in a subspace spanned by the ground and three excited electronic states. All trajectories were initiated from the first excited state and propagated for 800 fs or until the gap between the S_1 and S_0 states dropped below 0.15 eV which is taken as a good indicator of a nearby CI.[73,74]

2.2.3 Reaction path calculations. The use of a computationally very efficient, but not long-range corrected functional such as PBE0 leads to underestimation of charge transfer (CT) states. Therefore, TDDFT based NA dynamics is to be considered simply as a method for scrutinizing possible deactivation mechanisms. Reliable calculation of CT states can be performed using the ADC(2) method which was used to assess the feasibility of the main non-reactive relaxation mechanism encountered in the dynamics.[75] For the smaller system [*n*SBR$^+$TFA$^-$] ADC(2) optimization of the CI between two excited electronic states, S_1 and S_2, were performed using the sequential penalty constrained optimization method implemented in the CIOpt program.[76] The initial geometries were taken from the dynamics. By connecting a series of CIs we have obtained a low-lying S_2/S_1 CI. Furthermore, the Franck–Condon geometry and the S_2/S_1 CI were then joined in a linearly interpolated path. The energy profiles along the relaxation path were computed using the COSMO solvation model. The charge distribution of [*n*SBR$^+$TFA$^-$] in the lower (populated) excited state was taken as the one that polarizes the dielectric medium.

3 Results and discussion

3.1 Systems

The determination of the chromophore microenvironment is central for understanding the influence of the solvent on the lifetime of all-*trans* *n*SBR$^+$. Recent IR spectroscopy experiments in DCM in which the C/A ratio was gradually increased till 1 : 2 have proven that ionic aggregates with one, [*n*SBR$^+$TFA$^-$], and two counterions, [*n*SBR$^+$TFA$^-$]TFA, are formed in DCM, a non-polar solvent with low viscosity.[77]

Using the PBE0/TZVP method and COSMO solvation model we estimated that the 6s-*cis* form of *n*SBR$^+$ with the β-ionone ring twisted by 40° is 0.76 (0.41) kcal mol^{-1} more stable than the 6s-*trans* conformer in DCM (DMSO). We performed ground state molecular dynamics simulations of the two ion pairs of interest, [*n*SBR$^+$TFA$^-$] and [*n*SBR$^+$TFA$^-$]TFA starting from both the 6s-*cis* and 6s-*trans* forms of *n*SBR$^+$. In DCM, the 10 ps long production run of [*n*SBR$^+$TFA$^-$]TFA revealed large amplitude motion of the β-ionone ring with the $C_5{=}C_6$–$C_7{=}C_8$ dihedral angle varying between −73° and +85° in 6s-*cis* and between 119° and −134° in 6s-*trans* *n*SBR$^+$. The variation of the $C_{13}{=}C_{14}$ torsional angle in 6s-*cis* (6s-*trans*) was contained between 145° (154°) and −147° (−154°), while the fluctuations of the chromophore–counterion hydrogen bond were in the range 2.39 (2.38) Å $< d_{\mathrm{NO}} <$ 3.31 (3.51) Å. Thus, our simulations indicate that the dissociation of the ion pair is very unlikely in the electronic ground state. Similarly, only thermal fluctuations around the equilibrium hydrogen bond distance were observed in [*n*SBR$^+$TFA$^-$].

In the highly polar DMSO one expects the dissociation of the complex.[18] Indeed, from the time evolution of the [*n*SBR$^+$TFA$^-$] ion pairs in DMSO, shown in Fig. S1 (ESI†), it is evident that the ion-pair dissociates within few picoseconds. The dissociation also occurs in ACN (see Fig. S1, ESI†). Therefore we assumed that experiments performed in DMSO interrogated the relaxation dynamics of solvated, but isolated *n*SBR$^+$, while those performed in DCM addressed the chromophore–counterion pairs [*n*SBR$^+$TFA$^-$]TFA and [*n*SBR$^+$TFA$^-$].

3.2 Pump–probe measurements of the retinal chromophore–counterion pairs in solution

To investigate the role of the chromophore–counterion pair formation on the excited state dynamics of all-*trans* *n*SBR$^+$ we performed ultrafast pump–probe measurements in DCM and DMSO. Transient absorption spectra were collected in the standard pump–probe (PP) configuration for the C/A ratios of 1 : 1, 1 : 2 and 1 : 4. In DCM, the chromophore–counterion pair, [*n*SBR$^+$TFA$^-$], is formed for the C/A ratio of 1 : 1, while [*n*SBR$^+$TFA$^-$]TFA is formed for the C/A ratios of 1 : 2 and 1 : 4 as the excess TFA is likely to form cyclic hydrogen bonded dimers.[77,78] In the highly polar DMSO, no matter what is the C/A ratio, the formation of ion-pair is not possible.[18] Our spectral analysis (see ESI† text and Fig. S2–S10) and comparison with available time resolved fluorescence spectra (the data set was taken from a previous article[11]) allowed us to conclude that, for delays larger than 1 ps, the PP kinetic trace averaged over the 670 ± 5 nm range reflects the relaxation dynamics of the excited states. The high quality of data assured that the noise ($\sim 3 \times 10^{-4}$ OD) is 50 times lower than the maximum signal. As reported,[11] the band-shift happening in the first 1 ps cannot be ascribed to solvation but it is related to short lived bands related to higher vibrational states, and possibly to the S_2–S_0 emission (the 400 nm excitation can reach the S_2 state) which has sizeable oscillator strength due to mixing with S_1. On the other hand, the extra band appearing after 3 ps (best observed from 515 nm to 650 nm) is assigned, according to Bismuth *et al.* to metastable s-*cis* photoproducts.[79] Interestingly, as can be seen from Fig. S7 (ESI†), the extra band increase its intensity as the counterion concentration is increased.

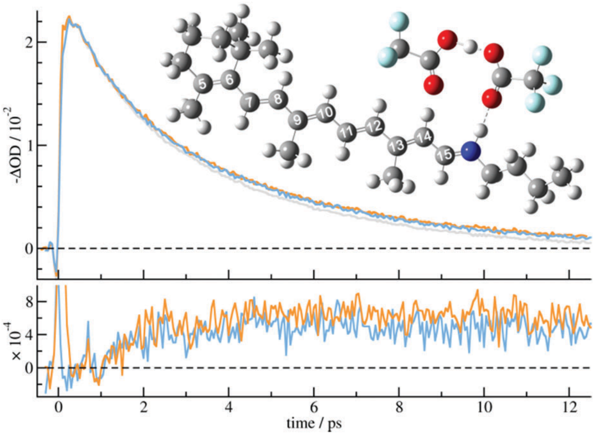

Fig. 1 (top) The normalized PP kinetic traces averaged over the 670 ± 5 nm range for three chromophore–counterion ratios: 1 : 1 grey, 1 : 2 blue, 1 : 4 ocher. (bottom) The differences between 1 : 2 and 1 : 1 traces (blue) and between 1 : 4 and 1 : 1 traces (ocher). The solvent is DCM. The inset shows the [*n*SBR$^+$TFA$^-$]TFA chromophore–counterion pair.

At the first glance the PP kinetic traces for the C/A ratios of 1 : 1, 1 : 2 and 1 : 4 shown in Fig. 1 (top) look rather similar. However, from the difference between the PP kinetic traces displayed in Fig. 1 (bottom) it is evident that the relaxation dynamics of the unshielded ion-pair [*n*SBR$^+$TFA$^-$] is faster than the relaxation dynamics of [*n*SBR$^+$TFA$^-$]TFA. For delays larger than 1 ps the difference between the 1 : 2 and the 1 : 1 traces (blue) and between the 1 : 4 and the 1 : 1 traces (ocher) is at least two times, and on average four times larger than the instrumental noise.

Although it is known that the excited state dynamics of *n*SBR$^+$ is multiexponential,[9–11,79,80] the PP kinetic traces averaged over the 670 ± 5 nm range were fitted with a monoexponential function for delays larger than 1 ps as only after that time delay the trace reflects the relaxation dynamics of the excited states. Such monoexponential fit provides information on how the average lifetime changes in function of the C/A ratio (see ESI†). The increase of the decay constant from $\tau_{1:1}$ = 3240 ± 20 fs to $\tau_{1:2}$ = 3355 ± 25 fs and $\tau_{1:4}$ = 3360 ± 20 fs in DCM implies that the average excited-state dynamics slows down by 4% in going from [*n*SBR$^+$TFA$^-$] to [*n*SBR$^+$TFA$^-$]TFA. No detectable change in the decay constants is found in going from the C/A ratio of 1 : 2 to 1 : 4. This is expected as the increase of the C/A ratio to 1 : 4 does not lead to formation of new species.

In contrast, the average excited state lifetimes of *n*SBR$^+$ in DMSO does not show any discernible trend when going from the ratio of 1 : 1 to 1 : 2 and finally to 1 : 5. Within the fit uncertainty, the decay constants $\tau_{1:1}$, $\tau_{1:2}$ and $\tau_{1:5}$ remain constant at 8950 ± 80 fs (Fig. 2).

3.3 Survey of possible non-reactive deactivation mechanisms in DCM

To uncover the molecular mechanism behind the sensitivity of the *n*SBR$^+$ lifetime on the counterion concentration in DCM, we investigated the excited state dynamics of the chromophore–counterion pairs [*n*SBR$^+$TFA$^-$] and [*n*SBR$^+$TFA$^-$]TFA. The PBE0/SVP//GAFF method was validated by computing vertical

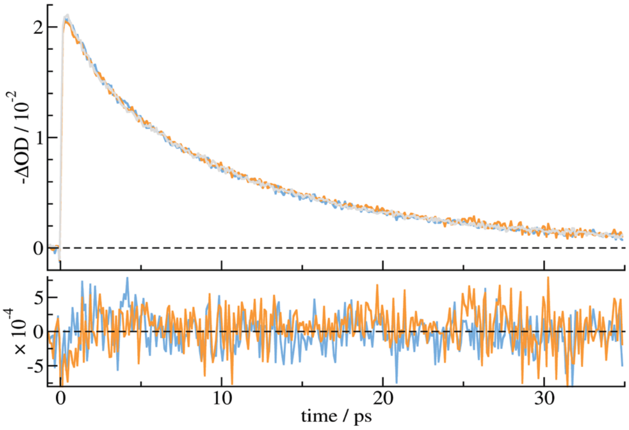

Fig. 2 (top) The normalized PP kinetic traces averaged over the 670 ± 5 nm range for three chromophore–counterion ratio: 1 : 1 grey, 1 : 2 blue, 1 : 5 ocher. (bottom) The differences between 1 : 2 and 1 : 1 traces (blue) and between 1 : 5 and 1 : 1 traces (ocher). The solvent is DMSO.

excitation spectra for an initial set of geometries sampled from room temperature ground state trajectories. For the allowed $S_0 \rightarrow S_1$ transition in [*n*SBR$^+$TFA$^-$] an excitation energy of 2.50 eV (496 nm) was obtained, while the absorption of [*n*SBR$^+$TFA$^-$]TFA was centered at 2.36 eV (526 nm). Both values agree very well with the redshift of the experimental absorption maximum from 2.67 eV (464 nm) to 2.43 eV (510 nm) observed in DCM when going from the equimolar ratio of the protonating acid to strong excess.[11]

For the same initial set of [*n*SBR$^+$TFA$^-$]TFA geometries additional calculations have been performed using the long-ranged corrected ωB97X-D functional. The ωB97X-D/SVP//GAFF absorption maximum was centered at 2.46 eV (505 nm), which is only slightly better than the PBE0/SVP//GAFF result. Thus, our electronic structure calculations confirm the stabilization of the S_1 state of [*n*SBR$^+$TFA$^-$]TFA with respect to [*n*SBR$^+$TFA$^-$]. Meanwhile, our measurements reveal a longer excited state lifetime of [*n*SBR$^+$TFA$^-$]TFA indicating that a barrier on the S_1 surface sensitive to the counterion charge may control the relaxation dynamics of the chromophore.[24,25]

As almost all available experimental results have been obtained in excess of protonating acid, we focus on [*n*SBR$^+$TFA$^-$]TFA. A total of 73 trajectories have been launched from the S_1 state and propagated in the manifold of the ground and three excited electronic states. During the 800 fs long simulation time 28 trajectories (38%) deactivated non-reactively to the ground electronic state, 27 of them *via* a counterion-sensitive mechanism that we tentatively assign to the fast non-reactive channel. The remaining 62% of the trajectories stayed in the $S_1(\pi\pi^*)$ state. For all 73 trajectories the distribution of initial energies is displayed in Fig. S11 (ESI†). The trajectories are further distributed into the set which deactivated to the ground state in the simulation time (red) and the one that remained in the excited state (blue). While the distribution of the total energies between the two sets is almost the same, the distribution of S_1 potential energy values shows that all trajectories in the first set have about 0.2 eV higher potential energy. This clearly indicates that the trajectories with higher excitation energy are more likely to deactivate to the ground electronic state and that indeed an energy barrier may be encountered on the way.

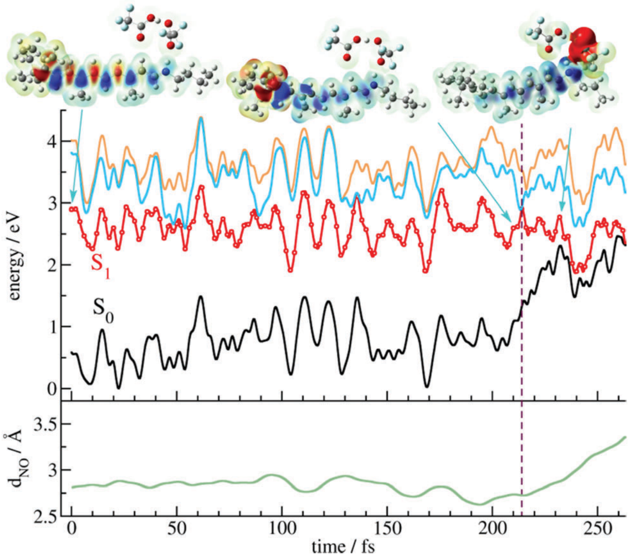

Fig. 3 Non-reactive relaxation of [*n*SBR$^+$TFA$^-$]TFA in DCM driven by the conical intersection between the intra-CT and inter-CT states. (top) Time dependence of the potential energy of the electronic ground state (S_0, black) and the first two excited singlet states (S_1, red; S_2, blue) for the selected nonadiabatic trajectory. The circles indicate the populated state at a given time. The insets show the electron density difference of the S_1 and S_0 states with areas of depletion (increase) of electron density in S_1 shown in red (blue). The character of the S_1 state changes from $\pi\pi^*$ (left) to intra-CT (middle) and inter-CT (right). The switch from intra-CT to inter-CT state at 214 fs (vertical line) is followed by the dissociation of [*n*SBR$^+$TFA$^-$]TFA. (bottom) Steep increase of the chromophore–counterion distance, d_{NO} on the inter-CT state. The computations have been performed at the PBE0/SVP//GAFF level, for details see Computational methods.

A nonadiabatic trajectory representative for the ensemble of trajectories displaying non-reactive deactivation of [*n*SBR$^+$TFA$^-$]TFA to the ground electronic state is shown in Fig. 3. Other trajectories illustrating [*n*SBR$^+$TFA$^-$]TFA and [*n*SBR$^+$TFA$^-$] deactivation are shown in the Fig. S13 and S14 (ESI†). Fig. S15 (ESI†) displays a characteristic trajectory that after 800 fs remained in the S_1 state.

Fig. 3 (top) shows the time variation of the potential energy of the ground (black line) and first two excited electronic states. The electronic state in which the system resides is indicated by red circles. In the initial geometry the β-ionone ring is rotated by −37.4° with respect to the *n*SBR$^+$ backbone, *i.e.*, the chromophore is in the 6s-*cis* form, and the N–H···O hydrogen bond length is 2.81 Å.

In the initially excited $S_1(\pi\pi^*)$ state the excitation is delocalized along the backbone. This is evident from the difference in the electron densities between S_1 and S_0 shown in the leftmost inset with red (blue) areas indicating depletion (increase) of electron density in S_1 with respect to S_0. The second excited state S_2 is also of $\pi\pi^*$ type as can be seen from the difference in the electron densities between S_2 and S_0 shown in Fig. S12 (ESI†).

These are the well-known ionic and covalent states, respectively. As expected, the motion of the system on the S_1 surface leads to migration of charge and strengthening of the intramolecular charge transfer (intra-CT) character of S_1 (middle inset). The elongation of the $C_5{=}C_6$ bond is the major geometrical change the system experiences in the intra-CT state. The activation of the backbone torsional angles was not observed. In the first 200 fs of the dynamics the S_1 and S_2 states approach each other in several occasions (50, 90, 140 fs) but the system remains in the ionic state. This is evident from the electron density differences show in Fig. S12 (ESI†). However, at 214 fs the system encounters a CI with an excited state of different character and a switch of states takes place. From the change in the electron density map (rightmost inset) it is evident that the new state corresponds to an inter-molecular CT state (inter-CT) in which the electron density is translocated from the carboxylic group of the TFA^- counterion to the Schiff base side of the chromophore. The intra-CT to inter-CT internal conversion is the key event in the deactivation of all-*trans* nSBR$^+$. The subsequent dissociation of the hydrogen bond between the chromophore and the counterion (Fig. 3 (bottom)) taking place on the inter-CT surface, strongly destabilizes the formally ionic ground electronic state of [nSBR$^+$TFA$^-$]TFA and leads within ~80 fs to the CI with the ground electronic state. From the absence of any torsional activation of the chromophore backbone we can safely conclude that the relaxation to the ground state is non-reactive.

Having described the role of the counterion in the deactivation of [nSBR$^+$TFA$^-$]TFA it is now useful to return to ensemble averages. Fig. S16a (ESI†) displays the distribution of the average CC bond lengths and the corresponding relative torsional angle changes of the nSBR$^+$ conjugated chain averaged over the entire length for each trajectory. The 28 trajectories that deactivate into the ground state over the intra-/inter-CT CI within the total simulation time are categorized separately from the remaining 45 trajectories that remained in the excited state by the end of the 800 fs dynamics. In general, the graphics clearly shows the difference in the bond stiffness between double (red) and single (blue) CC bonds in terms of their stretching and torsion. Trajectories deactivating through the intra-/inter-CT CI within the simulation time show a more significant change of bond lengths around the N-atom region due to the change in the local electronic density. In addition, the torsion of the $C_5{=}C_6{-}C_7{=}C_8$ angle is in average more pronounced compared to the set of trajectories remaining in the excited state, which displays larger torsions around the $C_{10}{-}C_{11}$ and $C_{12}{-}C_{13}$ single bonds. Distribution of the average N–H···O hydrogen bond lengths between the nSBR$^+$ and TFA^- ions is shown in Fig. S16b (ESI†). The difference in the hydrogen bond lengths is less pronounced between the two sets because the nSBR$^+$ and TFA^- are only free to move away from each other once the system is in the inter-CT state where the electrostatic interaction between the two species is significantly reduced, and because the separation process only happens after crossing the intra-/inter-CT CI before ending in the ground electronic state after about 65 fs. However, the average distance increase is still significant to be observed.

To investigate how the average lifetime changes in function of the chromophore acid ratio we have employed a monoexponential fit. In a previous article[12] we reported lifetimes of the fast and slow non-reactive mechanism of nSBR$^+$ in DCM of 1.0 ± 0.2 ps and 6.7 ± 0.7 ps, respectively as well as the relative amplitude of the two channels of 0.21 ± 0.03 and 0.35 ± 0.09. In our simulations 38% of trajectories deactivated to the ground state with and average deactivation tome of 318 fs. Thus, it is tempting to identify the counterion sensitive mechanism that emerged from our simulations as the fast non-reactive channel.

3.4 Reaction path study of retinal chromophore–counterion pair deactivation in DCM

It is known that TDDFT calculations underestimate the energies of CT states.[81] Although we are concerned with the relative ordering of two CT states, the proposed deactivation mechanism crucially depends on the accessibility of the intra-CT/inter-CT CI. Thus, we have investigated the CI region using the reference ADC(2) method.[45,46] Fig. 4 compares the potential energy of the ground and the lowest excited states at the ADC(2)/cc-pVDZ//GAFF (full line) and PBE0/SVP//GAFF (dashed line) levels. The results correspond to the trajectory displayed in Fig. 3, and are shown for the critical time window between 200 and 250 fs.

The spectroscopic intra-CT and inter-CT states are shown in red and blue, respectively. With respect to ADC(2), at the TDDFT level both, intra- and inter-CT states are underestimated by ~1.0 eV explaining the too fast relaxation observed in the TDDFT-based dynamics. However, the relative stabilization of the inter-CT state with respect to the intra-CT state is reproduced by the ADC(2) method. While the inter-molecular CT state may be indeed involved in the fast non-reactive relaxation of nSBR$^+$ in solution, further analysis is needed to confirm this assignment.

In particular, in the NA simulations the system follows the TDDFT gradient and explores regions of the potential energy surface that could be inaccessible to more accurate electronic structure methods. This means that a substantial barrier may

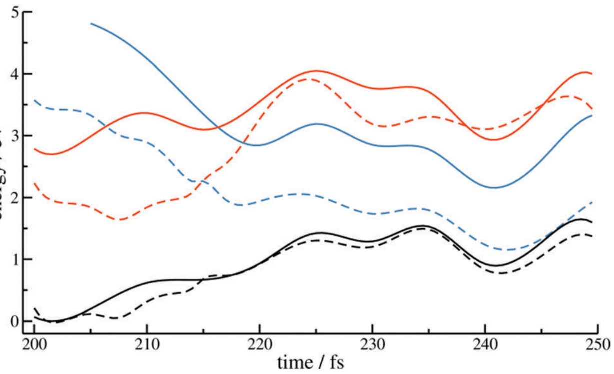

Fig. 4 Character of the electronic states near the intra-CT/inter-CT conical intersection. ADC(2)/cc-pVDZ//GAFF (solid) and PBE0/SVP//GAFF (dashed) energies of the intra-CT and inter-CT electronic states along the nonadiabatic trajectory shown in Fig. 3. Spectroscopic states of the same character are connected: ground state (black), intra-CT state (red), inter-CT state (blue).

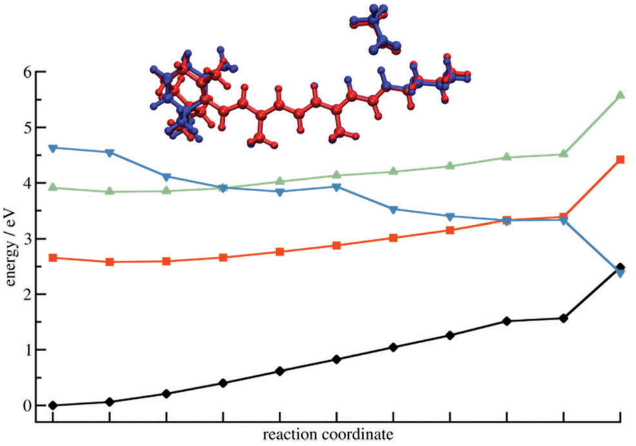

Fig. 5 Potential energy profiles along the linearly interpolated reaction path connecting the FC and the intra-CT/inter-CT CI geometries. The ground state and the two low-lying $\pi\pi^*$ states, S_1 and S_2 are shown in black, red and green, respectively. The inter-CT state is shown in blue. After the S_2/S_1 CI the inter-CT state polarizes the solvent and the CI with the ground state is reached almost immediately. The inset shows two overlapped [nSBR$^+$TFA$^-$] structures with β-ionone torsional angles of −50.1° (red) and 0.0° (blue).

separate the Franck–Condon (FC) and intra/inter-CT CI geometries at the ADC(2)/cc-pVDZ level. To investigate the accessibility of the intra-CT/inter-CT CI region we focus on the smaller system, [nSBR$^+$TFA$^-$]. Using geometries from dynamics simulation of the more stable 6s-*cis* form as initial guesses, a low lying intra-CT/inter-CT CI was obtained at the ADC(2) level. Fig. 5 displays the energy profiles of four electronic states along the reaction path connecting the intra-CT/inter-CT CI and FC geometry. The energies were evaluated in COSMO with the intra-CT state polarizing the dielectric. In the FC region the inter-molecular CT state is found as the third excited state, S_3. The state is strongly stabilized along this path and the intra-CT/inter-CT CI is reached 0.67 eV above the geometry of vertical excitation. The subsequent relaxation toward the electronic ground state is barrierless and reflects the sudden change of charge distribution in the chromophore which is used to polarize the solvent. The main geometry changes on the reaction path encompass the elongation of the chromophore–counterion distance from 1.45 to 2.25 Å and the out-of-plane motion of the Schiff base hydrogen atom monitored by a change of the C_{14}–C_{15}–N–H torsional angle from 0.54° to 11.4°. The orientation of the β-ionone ring ($\delta(C_5{=}C_6{-}C_7{=}C_8) = -50.1°$ at the FC geometry) is almost unchanged on the reaction path ($\delta(C_5{=}C_6{-}C_7{=}C_8) = -51.9°$ for S_2/S_1 CI). From ground state simulations, however, we know that the $\delta(C_5{=}C_6{-}C_7{=}C_8)$ angle easily varies between −70° and 80°. As a matter of fact two almost isoenergetic minima ($\Delta E = 0.19$ kcal mol^{-1}) characterized by torsional angles $\delta(C_5{=}C_6{-}C_7{=}C_8)$ of 45.2 and −50.1° have been optimized in the ground state. In the excited state we found that the orientation of the β-ionone ring influences the accessibility of the intra-CT/inter-CT CI. When the β-ionone ring lies in the plane of nSBR$^+$ backbone the ground state is destabilized, the FC geometry is higher in energy and the intra-CT/inter-CT CI is found only 0.42 eV above the FC geometry.

From the nature of the involved electronic states we can anticipate that the barrier to the intra-CT/inter-CT CI in [nSBR$^+$TFA$^-$]TFA would be larger in agreement with the observed faster decay of unshielded [nSBR$^+$TFA$^-$] ion-pair remarked in Fig. 1.

Finally the fact that a barrier is encountered on the non-reactive deactivation path of nSBR$^+$ in solution, agrees also with our previous measurements showing that the excitation on the blue edge (400 nm) of SBR$^+$ absorption leads to a decrease in the isomerization yield with respect to the excitation at the red edge (540 nm).[82] Altogether, our study provides a body of evidence that an inter-molecular CT state may be responsible for the fast non-reactive deactivation channel of nSBR$^+$ in non-polar solvents.

4 Conclusion

Pump–probe measurements, nonadiabatic dynamics simulations and reaction path calculations of all-*trans* nSBR$^+$ chromophore–counterion pairs have been used to identify the mechanisms that set in after photoexcitation of the retinal chromophore in non-polar solvents. We show for the first time that the electronic coupling between all-*trans* nSBR$^+$ and the hydrogen bonded counterion plays an important role in the retinal photodynamics in non-polar solvents. An ultrafast mechanism of non-reactive deactivation which includes excited state charge migration from the TFA$^-$ counterion to the retinal chromophore and subsequent dissociation of the ion-pair was identified. The mechanism provides a molecular-level explanation for the fast non-reactive relaxation channel experimentally observed in non-polar solvents.[12]

The photoisomerization of all-*trans* nSBR$^+$ in solution is a highly inefficient reaction. We hope that the present results will help to overcome this efficiency bottleneck.

Conflicts of interest

There are no conflicts to declare.

Acknowledgements

The authors thank Majed Chergui for kindly letting us reuse a data set from a previous article of one of our contributors. The research was supported by the Croatian Science Foundation under the project number 8238 and the COST action CM1204. The authors acknowledge generous computer time provided by the Croatian National Grid Infrastructure (CRONGI).

References

1 J. K. Lanyi, *Annu. Rev. Physiol.*, 2004, **66**, 665.
2 O. P. Ernst, D. T. Lodowski, M. Elstner, P. Hegemann, L. S. Brown and H. Kandori, *Chem. Rev.*, 2014, **114**, 126.
3 R. Mathies, C. Brito Cruz, W. Pollard and C. Shank, *Science*, 1988, **240**, 777.

4 S. Ruhman, B. Hou, N. Friedman, M. Ottolenghi and M. Sheves, *J. Am. Chem. Soc.*, 2002, **124**, 8854.
5 B. Schmidt, C. Sobotta, B. Heinz, S. Laimgruber, M. Braun and P. Gilch, *Biochim. Biophys. Acta*, 2005, **1706**, 165.
6 R. Govindjee, S. P. Balashov and T. G. Ebrey, *Biophys. J.*, 1990, **58**, 597.
7 K. A. Freedman and R. S. Becker, *J. Am. Chem. Soc.*, 1986, **108**, 1245.
8 H. Kandori and H. Sasabe, *Chem. Phys. Lett.*, 1993, **216**, 126.
9 P. Hamm, M. Zurek, T. Röschinger, H. Patzelt, D. Oesterhelt and W. Zinth, *Chem. Phys. Lett.*, 1996, **263**, 613.
10 G. Zgrablić, K. Voïtchovsky, M. Kindermann, S. Haacke and M. Chergui, *Biophys. J.*, 2005, **88**, 2779.
11 G. Zgrablić, S. Haacke and M. Chergui, *J. Phys. Chem. B*, 2009, **113**, 4384.
12 G. Zgrablić, A. M. Novello and F. Parmigiani, *J. Am. Chem. Soc.*, 2012, **134**, 955.
13 T. Sovdat, G. Bassolino, M. Liebel, C. Schnedermann, S. P. Fletcher and P. Kukura, *J. Am. Chem. Soc.*, 2012, **134**, 8318.
14 G. Bassolino, T. Sovdat, M. Liebel, C. Schnedermann, B. Odell, T. D. W. Claridge, P. Kukura and S. P. Fletcher, *J. Am. Chem. Soc.*, 2014, **136**, 2650.
15 G. Bassolino, T. Sovdat, A. S. Duarte, J. M. Lim, C. Schnedermann, M. Liebel, B. Odell, T. D. W. Claridge, S. P. Fletcher and P. Kukura, *J. Am. Chem. Soc.*, 2015, 150916112330003.
16 B. Loevsky, A. Wand, O. Bismuth, N. Friedman, M. Sheves and S. Ruhman, *J. Am. Chem. Soc.*, 2011, **133**, 1626.
17 I. Rivalta, A. Nenov and M. Garavelli, *Phys. Chem. Chem. Phys.*, 2014, **16**, 16865.
18 A. Muñoz-Losa, I. Fdez. Galván, M. A. Aguilar and M. E. Martín, *J. Chem. Theory Comput.*, 2013, **9**, 1548.
19 M. Garavelli, P. Celani, F. Bernardi, M. A. Robb and M. Olivucci, *J. Am. Chem. Soc.*, 1997, **119**, 6891.
20 R. Gonzalez-Luque, M. Garavelli, F. Bernardi, M. Merchan, M. A. Robb and M. Olivucci, *Proc. Natl. Acad. Sci. U. S. A.*, 2000, **97**, 9379.
21 M. Olivucci, A. Lami and F. Santoro, *Angew. Chem., Int. Ed. Engl.*, 2005, **44**, 5118.
22 M. Barbatti, M. Ruckenbauer, J. J. Szymczak, A. J. A. Aquino and H. Lischka, *Phys. Chem. Chem. Phys.*, 2008, **10**, 482.
23 O. Valsson and C. Filippi, *J. Chem. Theory Comput.*, 2010, **6**, 1275.
24 A. Cembran, F. Bernardi, M. Olivucci and M. Garavelli, *J. Am. Chem. Soc.*, 2004, **126**, 16018.
25 A. Cembran, F. Bernardi, M. Olivucci and M. Garavelli, *Proc. Natl. Acad. Sci. U. S. A.*, 2005, **102**, 6255.
26 I. Burghardt and J. T. Hynes, *J. Phys. Chem. A*, 2006, **110**, 11411.
27 J. P. Malhado and J. T. Hynes, *J. Chem. Phys.*, 2012, **137**, 22A543.
28 M. Ruckenbauer, M. Barbatti, T. Müller and H. Lischka, *J. Phys. Chem. A*, 2013, **117**, 2790.
29 C. Punwong, J. Owens and T. J. Martínez, *J. Phys. Chem. B*, 2015, **119**, 704.
30 n.d.
31 A. Klamt and G. Schuurmann, *J. Chem. Soc., Perkin Trans. 2*, 1993, 799.
32 S. Dapprich, I. Komáromi, K. S. Byun, K. Morokuma and M. J. Frisch, *J. Mol. Struct.: THEOCHEM*, 1999, **461–462**, 1.
33 T. Vreven and K. Morokuma, *J. Chem. Phys.*, 2000, **113**, 2969.
34 T. Vreven, K. S. Byun, I. Komáromi, S. Dapprich, J. A. Montgomery, K. Morokuma and M. J. Frisch, *J. Chem. Theory Comput.*, 2006, **2**, 815.
35 L. W. Chung, H. Hirao, X. Li and K. Morokuma, *Wiley Interdiscip. Rev.: Comput. Mol. Sci.*, 2012, **2**, 327.
36 J. P. Perdew, M. Ernzerhof and K. Burke, *J. Chem. Phys.*, 1996, **105**, 9982.
37 C. Adamo and V. Barone, *J. Chem. Phys.*, 1999, **110**, 6158.
38 A. Schäfer, C. Huber and R. Ahlrichs, *J. Chem. Phys.*, 1994, **100**, 5829.
39 T. H. Dunning Jr, *J. Chem. Phys.*, 1989, **90**, 1007.
40 J. P. Perdew, K. Burke and M. Ernzerhof, *Phys. Rev. Lett.*, 1996, **77**, 3865.
41 J. P. Perdew, K. Burke and M. Ernzerhof, *Phys. Rev. Lett.*, 1997, **78**, 1396.
42 W. D. Cornell, P. Cieplak, C. I. Bayly, I. R. Gould, K. M. Merz, D. M. Ferguson, D. C. Spellmeyer, T. Fox, J. W. Caldwell and P. A. Kollman, *J. Am. Chem. Soc.*, 1995, **117**, 5179.
43 D. A. Case, T. A. Darden, I. T. E. Cheatham, C. L. Simmerling, J. Wang, R. E. Duke, R. Luo, R. C. Walker, W. Zhang, K. M. Merz, B. Roberts, B. Wang, S. Hayik, A. Roitberg, G. Seabra, I. Kolossváry, K. F. Wong, F. Paesani, J. Vanicek, J. Liu, X. Wu, S. R. Brozell, T. Steinbrecher, H. Gohlke, Q. Cai, X. Ye, M.-J. Hsieh, G. Cui, D. R. Roe, D. H. Mathews, M. G. Seetin, C. Sagui, V. Babin, T. Luchko, S. Gusarov, A. Kovalenko and P. A. Kollman, *AMBER 2012*, University of California, San Francisco, 2012.
44 J. Wang, W. Wang, P. A. Kollman and D. A. Case, *J. Mol. Graphics Modell.*, 2006, **25**, 247.
45 J. Schirmer, *Phys. Rev. A: At., Mol., Opt. Phys.*, 1982, **26**, 2395.
46 A. B. Trofimov and J. Schirmer, *J. Phys. B: At., Mol. Opt. Phys.*, 1995, **28**, 2299.
47 C. Hättig, *Adv. Quantum Chem.*, 2005, **50**, 37.
48 A. Dreuw and M. Wormit, *Wiley Interdiscip. Rev.: Comput. Mol. Sci.*, 2015, **5**, 82.
49 N. O. C. Winter, N. K. Graf, S. Leutwyler and C. Hättig, *Phys. Chem. Chem. Phys.*, 2013, **15**, 6623.
50 S. Knippenberg, D. R. Rehn, M. Wormit, J. H. Starcke, I. L. Rusakova, A. B. Trofimov and A. Dreuw, *J. Chem. Phys.*, 2012, **136**, 64107.
51 A. Prlj, B. F. E. Curchod and C. Corminboeuf, *Phys. Chem. Chem. Phys.*, 2015, **17**, 14719.
52 J. Novak, A. Prlj, N. Basarić, C. Corminboeuf and N. Došlić, *Chem. – Eur. J.*, 2017, **23**, 8244.
53 D. Tuna, D. Lefrancois, Ł. Wolański, S. Gozem, I. Schapiro, T. Andruniów, A. Dreuw and M. Olivucci, *J. Chem. Theory Comput.*, 2015, **11**, 5758.
54 M. Persico, G. Granucci, S. Inglese, T. Laino and A. Toniolo, *THEOCHEM*, 2003, **621**, 119.
55 A. Toniolo, C. Ciminelli, G. Granucci, T. Laino and M. Persico, *Theor. Chem. Acc.*, 2004, **111**, 270.
56 S. Inglese, G. Granucci, T. Laino and M. Persico, *J. Phys. Chem. B*, 2005, **109**, 7941.

57 A. M. Virshup, C. Punwong, T. V. Pogorelov, B. A. Lindquist, C. Ko and T. J. Martínez, *J. Phys. Chem. B*, 2009, **113**, 3280.

58 M. Ruckenbauer, M. Barbatti, T. Müller and H. Lischka, *J. Phys. Chem. A*, 2010, **114**, 6757.

59 M. Wohlgemuth, V. Bonačić-Koutecký and R. Mitrić, *J. Chem. Phys.*, 2011, **135**, 54105.

60 O. Weingart, P. Altoè, M. Stenta, A. Bottoni, G. Orlandi and M. Garavelli, *Phys. Chem. Chem. Phys.*, 2011, **13**, 3645.

61 X. Li, L. W. Chung and K. Morokuma, *J. Chem. Theory Comput.*, 2011, **7**, 2694.

62 B. P. Fingerhut, S. Oesterling, K. Haiser, K. Heil, A. Glas, W. J. Schreier, W. Zinth, T. Carell and R. de Vivie-Riedle, *J. Chem. Phys.*, 2012, **136**, 204307.

63 J. C. Tully, *J. Chem. Phys.*, 1990, **93**, 1061.

64 M. J. Bearpark, F. Ogliaro, T. Vreven, M. Boggio-Pasqua, M. J. Frisch, S. M. Larkin, M. Morrison and M. A. Robb, *J. Photochem. Photobiol., A*, 2007, **190**, 207.

65 M. J. Bearpark, S. M. Larkin and T. Vreven, *J. Phys. Chem. A*, 2008, **112**, 7286.

66 E. Tapavicza, I. Tavernelli and U. Rothlisberger, *Phys. Rev. Lett.*, 2007, **98**, 23001.

67 I. Tavernelli, E. Tapavicza and U. Rothlisberger, *J. Chem. Phys.*, 2009, **130**, 124107.

68 R. Mitrić, U. Werner and V. Bonačić-Koutecký, *J. Chem. Phys.*, 2008, **129**, 164118.

69 J. Novak, M. Mališ, A. Prlj, I. Ljubić, O. Kühn and N. Došlić, *J. Phys. Chem. A*, 2012, **116**, 11467.

70 M. Mališ, Y. Loquais, E. Gloaguen, H. S. Biswal, F. Piuzzi, B. Tardivel, V. Brenner, M. Broquier, C. Jouvet, M. Mons, N. Došlić and I. Ljubić, *J. Am. Chem. Soc.*, 2012, **134**, 20340.

71 A. Prlj, N. Došlić and C. Corminboeuf, *Phys. Chem. Chem. Phys.*, 2016, **18**, 11606.

72 M. Mališ and N. Došlić, *Molecules*, 2017, **22**, 493.

73 M. Huix-Rotllant, M. Filatov, S. Gozem, I. Schapiro, M. Olivucci and N. Ferré, *J. Chem. Theory Comput.*, 2013, **9**, 3917.

74 S. Gozem, F. Melaccio, A. Valentini, M. Filatov, M. Huix-Rotllant, N. Ferré, L. M. Frutos, C. Angeli, A. I. Krylov, A. A. Granovsky, R. Lindh and M. Olivucci, *J. Chem. Theory Comput.*, 2014, **10**, 3074.

75 A. A. J. Aquino, I. Borges, R. Nieman, A. Köhn and H. Lischka, *Phys. Chem. Chem. Phys.*, 2014, **16**, 20586.

76 B. G. Levine, J. D. Coe and T. J. Martínez, *J. Phys. Chem. B*, 2008, **112**, 405.

77 N. Biliškov, J. Novak, M. Petković, G. Zgrablić, G. Baranović and N. Došlić, *Croat. Chem. Acta*, 2011, **84**, 221.

78 T. Takamuku, Y. Kyoshoin, H. Noguchi, S. Kusano and T. Yamaguchi, *J. Phys. Chem. B*, 2007, **111**, 9270.

79 O. Bismuth, N. Friedman, M. Sheves and S. Ruhman, *Chem. Phys.*, 2007, **341**, 267.

80 B. Hou, N. Friedman, S. Ruhman, M. Sheves and M. Ottolenghi, *J. Phys. Chem. B*, 2001, **105**, 7042.

81 A. Dreuw and M. Head-Gordon, *Chem. Rev.*, 2005, **105**, 4009.

82 G. Zgrablić, M. Ricci, A. M. Novello and F. Parmigiani, *Photochem. Photobiol.*, 2010, **86**, 507.